International Journal of Biological Macromolecules 158 (2020) 305–317

Contents lists available at ScienceDirect

International Journal of Biological Macromolecules

journal homepage: http://www.elsevier.com/locate/ijbiomac

Structural features of $HtpG_{Mtb}$ and HtpG-$ESAT6_{Mtb}$ vaccine antigens against tuberculosis: Molecular determinants of antigenic synergy and cytotoxicity modulation

Miguel Moreira [a,1], Alessia Ruggiero [a,1], Luciana Esposito [a], Han-Gyu Choi [b], Hwa-Jung Kim [b], Rita Berisio [a,*]

[a] Istituto di Biostrutture e Bioimmagini, C.N.R., Via Mezzocannone 16, I-80134 Napoli, Italy
[b] Department of Microbiology, and Medical Science, College of Medicine, Chungnam National University, Daejeon, Republic of Korea

ARTICLE INFO

Article history:
Received 28 February 2020
Received in revised form 18 April 2020
Accepted 28 April 2020
Available online 04 May 2020

Keywords:
Protein structure
Vaccine
Chaperone
Tuberculosis
Conformation
Ligand binding

ABSTRACT

Vaccine development against tuberculosis is an urgent need as the only available vaccine, *M. bovis* Bacillus Calmette Guerin (BCG), is unable to provide significant protection in adults. Among newly identified antigens, Rv2299c is an excellent candidate for the rational design of an effective multi-antigenic TB vaccine. Also, when fused to the T cell antigen ESAT6, it becomes highly effective in boosting BCG immunization and it adopts low cytotoxicity compared to ESAT6.

We here characterize these proteins by coupling various biophysical techniques to cytofluorimetry and computational studies. Altogether, our data provide an experimental evidence of the role of Rv2299c as a dimeric and highly thermostable molecular chaperone, here denoted as $HtpG_{Mtb}$. Molecular dynamics simulations show that ATP rigidly anchors the ATP-binding loop in a conformation incompatible with the structure of the free enzyme. We also show that $HtpG_{Mtb}$ dimeric state is an important molecular feature for the improved antigenic and cytotoxic properties of HtpG-$ESAT6_{Mtb}$. Indeed, structural features of HtpG-$ESAT6_{Mtb}$ show that not only does this molecule combine the antigenic properties of $HtpG_{Mtb}$ and ESAT6, but $HtpG_{Mtb}$ locks ESAT6 in a dimeric state, thus improving its cytotoxicity properties. The data presented here provide solid basis for the rational design of upgraded antigens.

1. Introduction

Mycobacterium tuberculosis (Mtb) is the organism causative of tuberculosis (TB), an infectious disease that generally affects the lungs but that can spread to other parts of the body [1–3]. In addition, Mtb is able of extrapulmonary dissemination, using Heparin Binding Haemagglutinin Adhesin (HBHA), a dimeric protein which enables Mtb to bind to sulphated glycoconjugates on epithelial cells [4,5]. Mtb is one of the most proficient pathogens as it is latent on around a quarter of the world population (1,7 billion people) and kills about 5 thousand people every day (World Health Organization report 2019). Only 5% to 10% of the individuals infected with the latent Mtb will develop the disease [6,7], through the resuscitation of dormant bacteria operated by Resuscitation Promoting Factors [8–16]. However, a combination of high infectiousness [1–3], low effectiveness of vaccination [17–20] and the existence of multidrug resistances to existing treatments [6,21] keeps TB a global emergency, as defined by the WHO.

Even though several drug treatments are available for TB, success rates vary from 84% for susceptible to only 54% multi-drug resistant TB [6,21]. Therefore, it is of the utmost importance to prevent the spread and infection of Mtb. Notwithstanding, being the only commercially available vaccine against Mtb, the BCG (*M. bovis* Bacillus Calmette Guerin) is not effective in population immunization (0% to 80% efficacy in adults and approximately 50% efficacy in children). Hence, there is a strong need to develop new immunization mechanisms for TB either as standalone vaccines or to boost the currently commercialized BCG [22].

A promising strategy in TB vaccine development is to identify vaccine adjuvants, which boost BCG vaccines [22]. The identification and characterization of new mycobacterial antigens is key to the effective development of heterologous TB vaccine candidates. Based on comparative genomics analysis, a chromosomal region of difference (RD1) has been identified in all virulent members of Mtb and *Mycobacterium bovis* but not in live attenuated vaccine strains of Bacille Calmette-Guerin (BCG), neither in avirulent mycobacteria such as *Mycobacterium microti* [23,24]. RD1 encodes a secretion complex, ESX-1, of which key effectors are the early-secreted antigenic target-6 kDa (ESAT6) and the culture

Abbreviations: Mtb, *Mycobacterium tuberculosis*; TB, Tuberculosis; WHO, World Health Organization; DC, dendridic cell; PDB, Protein Databank; ASB, amidosulfobetaine; BCG, Bacillus Calmette Guerin; Hsp, Heat shock protein; MD, molecular dynamics; RMSD, root means square deviation; RMSF, root mean square fluctuation.

* Corresponding author.
E-mail address: rita.berisio@cnr.it (R. Berisio).

[1] These authors equally contributed to this work.

https://doi.org/10.1016/j.ijbiomac.2020.04.252
0141-8130/

filtrate protein 10 kDa (CFP10) [25,26]. In a previous work, we tested the hypothesis to couple ESAT6 with protein antigens which activate dendritic cells (DC), so to improve the long-term efficacy vaccines containing only T-cell antigens, as ESAT6 is. In particular, we found that the protein Rv2299c, here denoted as $HtpG_{Mtb}$, effectively induced DC maturation and possessed antimycobacterial action through DC activation [27]. Also, a fusion protein between $HtpG_{Mtb}$ and ESAT6 was effective in boosting BCG immunization [27]. Despite the importance of $HtpG_{Mtb}$ as an excellent candidate for the rational design of an effective multiantigenic TB vaccine, no structural information on this protein is hitherto available.

To address this and related questions, we have investigated the structural properties of $HtpG_{Mtb}$ and HtpG-$ESAT6_{Mtb}$, using a plethora of experimental methods. To gain more detailed structural information from the experimental data, we have also carried out molecular modeling and dynamics studies. Altogether, our data show that $HtpG_{Mtb}$ is a highly stable, albeit highly flexible, dimeric protein. Consistent with sequence predictions, our results suggest that $HtpG_{Mtb}$ acts as a molecular chaperone whose structure strongly correlates with its functional state. In addition, our data provide a rational to the improved cytotoxic properties of the fused HtpG-$ESAT6_{Mtb}$ antigen. Besides being important for understanding of functional aspects of a key protein of Mtb, this study sets the basis to the structure-based design of improved antigens, active as TB vaccine boosters.

2. Materials and methods

2.1. Recombinant production of $HtpG_{Mtb}$ and HtpG-$ESAT6_{Mtb}$

Cloning, expression and purification were performed according to [27]. Briefly, BL21(DE3) transformed cells were used to express the recombinant protein using 0.5 mM IPTG as inducer at 18 °C. Cell pellets we re-suspended in 30 mL binding buffer (50 mM Tris-HCl pH 8.0, 300 mM NaCl, 5% (v/v) glycerol, 2 mM DTT), supplemented with a protease-inhibitor cocktail (Roche Diagnostic), and sonicated for 10′. The lysate was cleared by centrifugation at 35,000g, and the supernatant was loaded on Ni^{2+}-NTA resin (Qiagen) equilibrated with binding buffer.

Three washing steps with 10 volumes of binding buffer were performed with increasing concentrations of imidazole (10, 20 and 40 mM). $HtpG_{Mtb}$ was eluted with 150 mM of imidazole. After elution, the protein was dialyzed against 50 mM Tris-HCl pH 8.0, 50 mM NaCl, 2 mM DTT, and 5 mM EDTA at 4 °C. In order to remove bound nucleic acids from $HtpG_{Mtb}$, the dialyzed protein was loaded on an anionic exchange chromatography using a 5 mL HiTrap Q HP (GE Healthcare). The protein was eluted by applying a gradient of NaCl (50 mM to 2 M). Finally, the protein was further purified by size exclusion chromatography on Superdex 200 16/60 (GE Healthcare) (50 mM Tris-HCl pH 8.0, 150 mM NaCl, 2% (v/v) glycerol, 2 mM DTT). The protein eluted in a single peak and was homogeneous as judged by SDS–PAGE analysis and mass spectrometry (74,480 Da). HtpG-$ESAT6_{Mtb}$ was produced with the same approach.

2.2. Mass spectrometry

Molecular masses of $HtpG_{Mtb}$ and HtpG-$ESAT6_{Mtb}$ were checked by mass-spectrometry. MS analysis was performed on an LCQ DECA XP Ion Trap mass spectrometer (ThermoElectron, Milan, Italy) equipped with an OPTON ESI source (operating at 4.2-kV needle voltage and 320 °C), and with a complete Surveyor HPLC system. Narrow bore 50 × 2 mm C18 BioBasic LC-MS columns (ThermoElectron) were used for the analyses. LC binary gradient was from 5% to 70% of B (where B was CH3CN 0.05% TFA, and A H2O 0.08% TFA) in 45 min. Initial protein concentration was 1.3 μM (0.1 mg/mL). 2 μL of this solution was injected for all analyses. Mass spectra were recorded continuously between the mass range 400–2000 Da in positive mode. Multicharge spectra were deconvoluted using the BioMass program implemented in the Bioworks 3.1 package provided by the manufacturer.

2.3. Circular dichroism

All CD spectra were recorded with a Jasco J-810 spectropolarimeter equipped with a Peltier temperature control system (Model PTC-423-S). Molar ellipticity per mean residue, [θ] in deg. $cm^2 \cdot dmol^{-1}$, was calculated from the equation: $[\theta] = [\theta]_{obs} \cdot mrw \cdot (10 \cdot l \cdot C)^{-1}$, where $[\theta]_{obs}$ is the ellipticity measured in degrees, mrw is the mean residue molecular mass (112 Da), *C* is the protein concentration in $g \cdot L^{-1}$ and *l* is the optical path length of the cell in cm. Far-UV measurements (190–260 nm) were carried out at 20 °C using a 0.1 cm optical path length cell and a protein concentration of 0.15–0.2 $mg \cdot mL^{-1}$. The protein samples were prepared diluting the protein in 20 mM sodium phosphate buffer (pH 7.4). Thermal denaturation studies were performed by recording the CD signal at 222 nm from 20 °C to 100 °C.

2.4. Static and dynamic light scattering experiments

For static light scattering (SLS), a MiniDAWN™ Treos spectrometer (Wyatt Instrument Technology Corp.) equipped with a laser operating at $\lambda = 658$ nm was used connected on-line to a size-exclusion chromatography. Purified protein was analyzed by size-exclusion chromatography connected to a triple-angle light scattering detector equipped with a QELS module (quasi-elastic light scattering) for molar mass evaluation. 500 μg of sample were loaded on a S75 10/300 (GE Healthcare) column, equilibrated in 50 mM Tris-HCl pH 8.0, 150 mM NaCl, 5% (v/v) glycerol, 2 mM DTT. A constant flow rate of 0.5 mL min^{-1} was applied. Elution profiles were detected by a Shodex interferometric refractometer and a MiniDAWN™ Treos light scattering system. Data were analyzed by using Astra 5.3.4.14 software (Wyatt Technology, Toulouse, France).

Dynamic Light scattering for size measurements as a function of temperature were performed on a Zetasizer, Malvern Nano-ZS spectrometer. The wavelength of the laser was 632.8 nm, and the scattering angles 90° and 175°. Protein sample diluted to 1 mg/mL in 10 mM sodium phosphate (pH 7.4) and analyzed in a temperature range between 20 °C and 45 °C. The hydrodynamic radius (Rh) is calculated from the autocorrelation function of the intensity of light scattered from the particles assuming a spherical form of particles. For each sample, the mean value of particles diameters was calculated from five replicate determinations.

2.5. Homology modeling

The homology model structures of $HtpG_{Mtb}$ in the different binding states were obtained after consensus-based sequence alignment using the HHpred tool. For the three binding states of the enzyme, we chose the following template models: (i) the structures of *E. coli* HtpG for the apo and ADP-bound states showing 46% sequence identity on 619 residues (PDB codes: apo state 2ioq - 3.5 Å resolution); ADP-bound state (PDB codes: 2iop - residues 1–624, 3.55 Å resolution/2ior - residues 1–211, 1.65 Å resolution); (ii) the structure of *Saccharomyces cerevisiae* Hsp90 in the AMP-PNP bound state showing 39% sequence identity on 631 residues (PDB code: 2cg9–3.1 Å resolution). Using these alignments, the structures were built using the program MODELLER [28]. The fused HtpG-$ESAT6_{Mtb}$ protein was modelled in the ATP bound state. The ESAT6 portion of the structure was modelled using the crystal structure of the ESAT6-CFP10 complex from Mtb (PDB code 3FAV) as a template. The linker between $HtpG_{Mtb}$ and ESAT6 was modelled in an extended conformation.

2.6. Molecular dynamics

Simulations were performed by the GROMACS package [29], using protocols already tested for other protein systems [30,31]. For each starting model (residues 1–419), MD simulations were carried out using the Amber99sb all-atom force field [32,33] with tip3p water model. All simulations were run in the isobaric-isothermal (NPT) ensemble at 300 K, using periodic boundary condition.

The starting models were solvated in a dodecahedron box with minimal distance of the model to the box wall of 1.1 nm. Sodium ions were added by replacing water molecules to neutralize the overall charge. Details are listed in Table S1. Before starting MD simulations, the systems were subjected to energy minimization and then, the solvent was equilibrated first in NVT and then in NPT ensemble for 100 ps, during which the protein atoms were restrained to the energy-minimized initial coordinates. Subsequently, the thermalization process consisted of a sequence of 100 ps runs where the temperature was increased from 50 K to 300 K in 50 K steps. At this stage the Berendsen method for pressure control was used with a coupling constant $\tau_p = 1.0$ ps, whereas the temperature was kept constant at 300 K by the V-rescale method with a $\tau_t = 0.1$ ps. The integration time step was 0.002 ps and LINCS was the constraint algorithm used [34]. A cut-off of 10 Å was used for the treatment of both electrostatic and Lennard-Jones interactions. The Particle Mesh Ewald (PME) was used for the long-range interactions [35]. For the 500 ns production run we switched to the Parrinello-Rahman method to keep the pressure at 1 bar with a coupling constant $\tau_p = 2.0$ ps. All the trajectories were analyzed using GROMACS routines. Structural properties, such as root mean-square deviation (RMSD), root mean-square fluctuation (RMSF), secondary structure (SS), were calculated with GROMACS or Visual Molecular Dynamics (VMD) [36] standard analysis tools. We used the Amber parameters for both ADP and ATP molecules archived by Richard Bryce (University of Manchester, UK) [37].

To answer the question of whether binding of ADP is compatible with the conformation of the enzyme observed in the free state, we conducted MD studies integrated with clustering analysis. Namely, we first performed extensive (1 μs) MD simulations of the sole catalytic domain of $HtpG_{Mtb}$ (residues 1–219) in complex with ADP. The starting homology model for this MD was obtained using the high resolution structure of *E. coli* ADP bound domain (PDB code 2IOR, 1.65 Å resolution). Then, we performed a clustering procedure of this trajectory data by using the ptraj module of Amber. We selected the backbone atoms (N, CA, C) of all 219 residues of the structure. The equilibrated part of the trajectory (300–1000 ns) sampled every 5 ps was used for the clustering. We searched for five clusters by the means algorithm using a mass-weighted RMS metric to compare all the selected atoms. The major cluster, representing 83% of sampled structures, was used to build a starting model for the MD simulation of $HtpG_{Mtb}$ carrying the ADP bound catalytic domain (1–419 residue) in the framework of a free-like conformation of $HtpG_{Mtb}$. To achieve this, residues of the catalytic domain in the homology model of free $HtpG_{Mtb}$ were replaced with the obtained major cluster structure. MD simulations were then performed with the same procedure described for free and ATP bound structures. All simulations were analyzed using in-house programs and analysis tools from the GROMACS package [29]. RMSF were calculated on an equilibrated part of the trajectories, including the last 400 ns.

2.7. Preparation of macrophage cells

Bone marrow cells isolated from C57BL/6 mice were lysed with red blood cell (RBC)-lysing buffer (ammonium chloride 4.15 g/500 mL, 0.01 M Tris-HCl buffer pH 7.5 ± 2) and washed with the DMEM medium. The obtained bone marrow derived macrophage cells (BMDM) were plated in six-well culture plates (10^6 cells/mL, 3 mL/well) and cultured at 37 °C in the presence of 5% CO_2 in DMEM media supplemented with 100 unit/mL penicillin/streptomycin (Lonza), 10% of fetal bovine serum (Lonza), 50 μM mercaptoethanol (Lonza), 0.1 mM nonessential amino acids (Lonza), 1 mM sodium pyruvate (Sigma), 20 ng/mL M-CSF.

2.8. Cytotoxicity analysis

BMDM (10^5) were incubated with either 5 μg/mL ESAT-6, Rv2299c-ESAT-6 or Rv2299c alone. In parallel, BMDM (10^5) were incubated with each antigen after (a) boiling them for 30 min at 100 °C or (b) mixing them with 0.0005% amidosulfobetaine (ASB, Sigma) buffer. Stausporin (STS) and ASB were used as controls. After 24 h, cytotoxicity analysis was conducted using an Annexin V/propidium iodide (PI) staining kit (BD Biosciences). Analysis of the stained cells was performed on a FACSCanto II with FACSDiva, and the results were analyzed using the FlowJo software (Tree Star, Ashland, OR, USA).

2.9. Native gel electrophoresis

10 μg of purified proteins were diluted in a non-reducing non-denaturing sample buffer (50 mM Tris HCl, pH 8.6, 8% glycerol, and 0.0025% bromophenol blue) in the presence and in absence of ASB. ASB was added in protein:ASB molar ratios from 1:100 to 1:400. Protein separation was performed on a 10% Polyacrylamide NATIVE-gel for 2–3 h at 80 V. Both the running buffer (Tris-Glycine Buffer) and the gel were kept cold.

3. Results

3.1. Structural features of $HtpG_{Mtb}$ and HtpG-$ESAT6_{Mtb}$ in solution

In $HtpG_{Mtb}$ sequence, two distinct domains can be identified in the Protein Family database PFAM (Fig. 1A). The N-terminal domain is a predicted catalytic GHKL (Gyrase, Hsp90, Histidine Kinase, MutL) domain (residues 26–184), an evolutionary conserved ATPase domain shared by histidine kinase, DNA gyrase B and Hsp90. Differently, the C-terminal domain (224–647) is typical only of the Hsp90 family, a class of large chaperone proteins (about 90 kDa). Hsp90, which stands for Heat shock protein 90, assists protein folding in eukaryotes and stabilizes proteins against heat stress [38,39]. Instead of Hsp90, prokaryotes have HtpG (High temperature protein G) that, similar to eukaryotic Hsp90, are molecular chaperones with ATPase activity. In *E. coli*, this protein has also recently been shown to be a modulator of cell division by protecting from degradation FtsZ, an almost universally conserved GTP-ase involved in septal ring formation [40,41]. Sequence analysis with BLASTP shows that $HtpG_{Mtb}$ shares 46% sequence identity with the HtpG of *Escherichia coli* (PDB code 2IOP), a finding which suggests a similar function for $HtpG_{Mtb}$. We coupled analytical size-exclusion chromatography (SEC) with multi-angle light scattering (MALS) to investigate the oligomerization state of $HtpG_{Mtb}$ in solution. The on-line measurement of the intensity of the Rayleigh scattering as a function of the angle as well as the differential refractive index of the eluting peak in SEC was used to determine the molecular weight (MW). This analysis produced MW values which correspond to a dimeric species (MW 145.2 ± 0.6 kDa, Fig. 1B). Using far-UV CD spectroscopy, we observed that the spectrum of $HtpG_{Mtb}$ is typical of a well-structured fold with a high α-helical content (Fig. 1C). Spectra in Fig. 1C also show that folding is almost fully reversible and that the enzyme is endowed with elevated stability, as the CD spectrum recorded at 100 °C still presents some level of structural content (Fig. 1C). The same analysis was conducted for the fused antigen HtpG-$ESAT6_{Mtb}$, which embeds a linker between $HtpG_{Mtb}$ and ESAT6, due to the cloning strategy (Fig. 1A). Similar to $HtpG_{Mtb}$, HtpG-$ESAT6_{Mtb}$ has a dimeric structure (MW 172.1 ± 0.3 kDa, Fig. 1B). CD spectra of the two proteins also

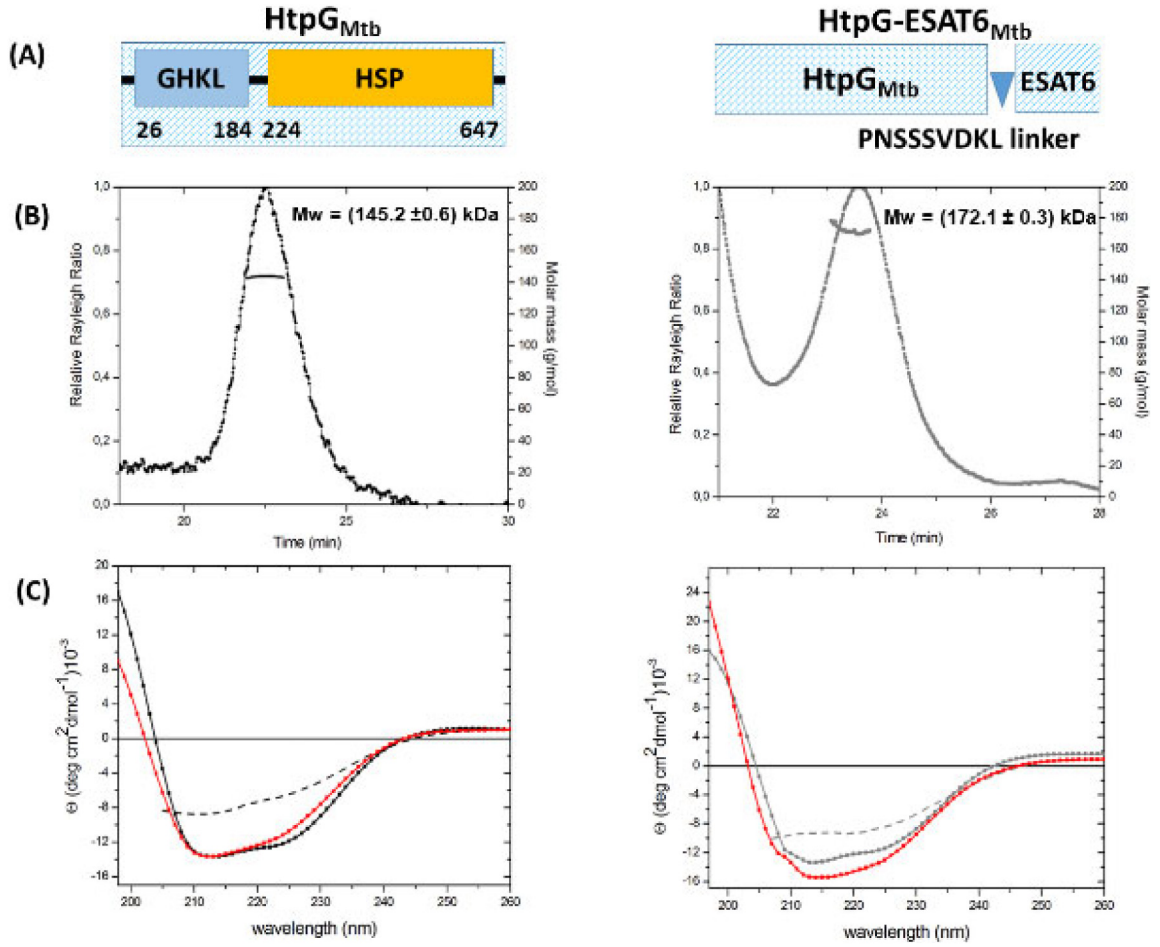

Fig. 1. HtpG$_{Mtb}$ and HtpG-ESAT6$_{Mtb}$ are well folded dimeric proteins. (A) A schematic view of HtpG$_{Mtb}$ (left) and HtpG-ESAT6$_{Mtb}$ (right) domain organization. (B) Analytical SEC-MALS of (left) and HtpG-ESAT6$_{Mtb}$ (right); black curves represent the Rayleigh ratio (left scale) against the retention time. Molecular mass (right scale) values correspond to a dimeric state. (C) CD of HtpG$_{Mtb}$ (left) and HtpG-ESAT6$_{Mtb}$ (right) in 20 mM sodium phosphate, pH 7.4. Spectra are reported for measurements at 20 °C (red), at 100 °C (dotted black) and after refolding (black).

show similar profiles (Fig. 1C), consistent with the small size of the ESAT6 domain (95 residues) compared to that of HtpG$_{Mtb}$ (647 residues).

To investigate the heat-induced changes in the protein secondary structure, thermal unfolding curves of both HtpG$_{Mtb}$ and HtpG-ESAT6$_{Mtb}$ were recorded by following the CD signal at 222 nm as a function of temperature, using a 1 °C/min heating rate. Thermal unfolding curves at pH 7.4 show that two transitions exist, the first (T_{mon}) close to 40 °C, and likely corresponding to the monomerization of the enzyme (Fig. 2), the second due to unfolding, T_m. Whereas T_{mon} of HtpG$_{Mtb}$ and HtpG-ESAT6$_{Mtb}$ are comparable, a significant difference exists between T_m values, with HtpG-ESAT6$_{Mtb}$ slightly more stable than HtpG$_{Mtb}$ (Tm 88 °C versus 81 °C, Fig. 2).

To corroborate that the transition at T_{mon} is an event associated to monomerization, we performed Dynamic Light scattering studies of HtpG$_{Mtb}$ as a function of temperature. As shown in Fig. 3A, we observe a significant decrease of HtpG$_{Mtb}$ hydrodynamic radius from 6.7 ± 0.4 nm at 20 °C to 4.4 ± 0.5 nm at 45 °C. This result confirms, as suggested by CD unfolding studies (Fig. 2), that the unfolding process of HtpG$_{Mtb}$ occurs in two steps, and involves the formation of highly stable monomers. The decrease of the hydrodynamic radius of HtpG$_{Mtb}$ is observed also in the presence of AMP-PNP, from 6.5 ± 0.3 nm at T of 20 °C to 4.4 ± 0.3 nm at 45 °C (Fig. 3B). In this case, all measurements present significantly lower standard deviations, a finding that witnesses a more homogeneous distribution of molecular dimensions. This finding is indicative of a less flexible structure of the protein in the presence of AMP-PNP, as discussed below.

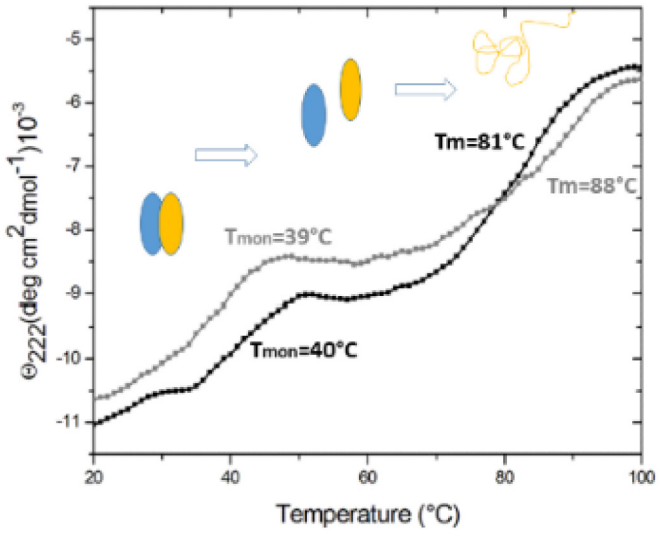

Fig. 2. HtpG$_{Mtb}$ monomerizes prior to unfolding. CD denaturation curves measured at 222 nm for HtpG$_{Mtb}$ (black) HtpG-ESAT6$_{Mtb}$ (grey). Monomerization (T_{mon}) and melting temperatures (T_m) are reported with corresponding colors.

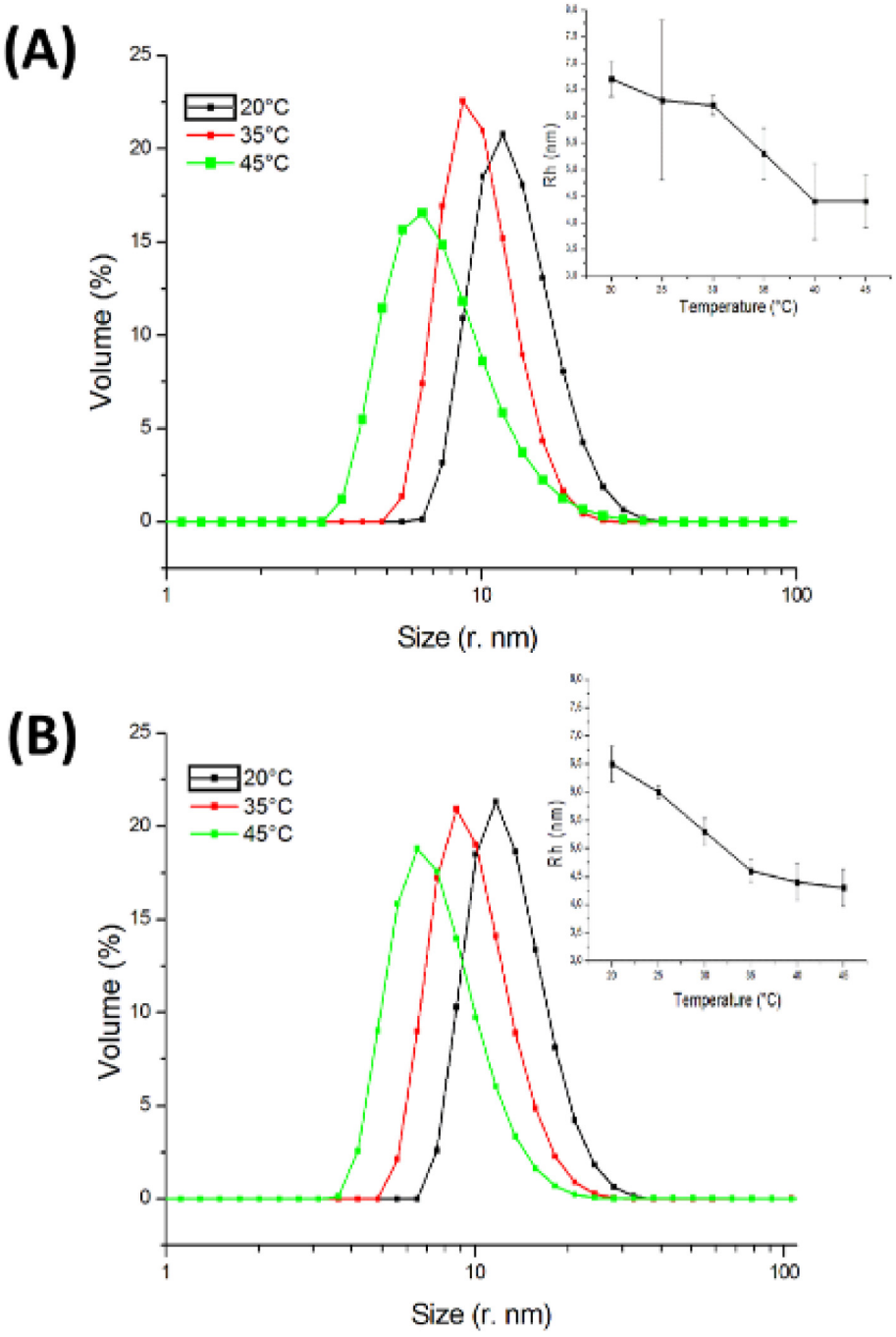

Fig. 3. Dynamic light scattering studies. DLS measurements a function of temperature for (A) $HtpG_{Mtb}$ and (B) $HtpG_{Mtb}$ in the presence of AMP-PNP. Curves report distributions of hydrodynamic radii (Rh) at the reported temperatures. The computed Rh and standard deviations are reported in the insets.

3.2. Homology modeling in different functional states

Using the available structural data in the PDB, we computed homology models of $HtpG_{Mtb}$ in all its binding states, including its free form, its ATP bound form and its ADP bound form. All models are fully reliable, based on sequence identity with their templates [38,42] and on a series of validation tools we applied (see Materials and methods). As shown in Fig. 4, enormous conformational changes are associated to binding of ATP and to its hydrolysis to ADP (Fig. 4). Consistent with CD unfolding data and with light scattering results (Figs. 2 and 3), all forms are dimeric. Each monomer is constituted, beside the N-terminal catalytic domain, of a middle and a C-terminal domain, with their orientations differing in the three functional states (Fig. 4). In the free state, the two monomers are bound together solely by their C-terminal domains, a finding which well agrees with the conformational flexibility suggested by the wider range of hydrodynamic radii measure by DLS (Figs. 3, 4A). On analogy with other Hsps [38,39], this open state is characterized by full accessibility of both the catalytic and the middle domains to host the client proteins that need to be assisted in their folding process. By contrast, the ATP bound state is fully compact, with both the C-terminal and the catalytic domains involved in the dimerization process (Fig. 4B). Indeed, differences between the homology models of the free and ATP bound $HtpG_{Mtb}$ also include the swapping of the N-terminal strands, to obtain a fully compact ATP bound dimer (Fig. 4).

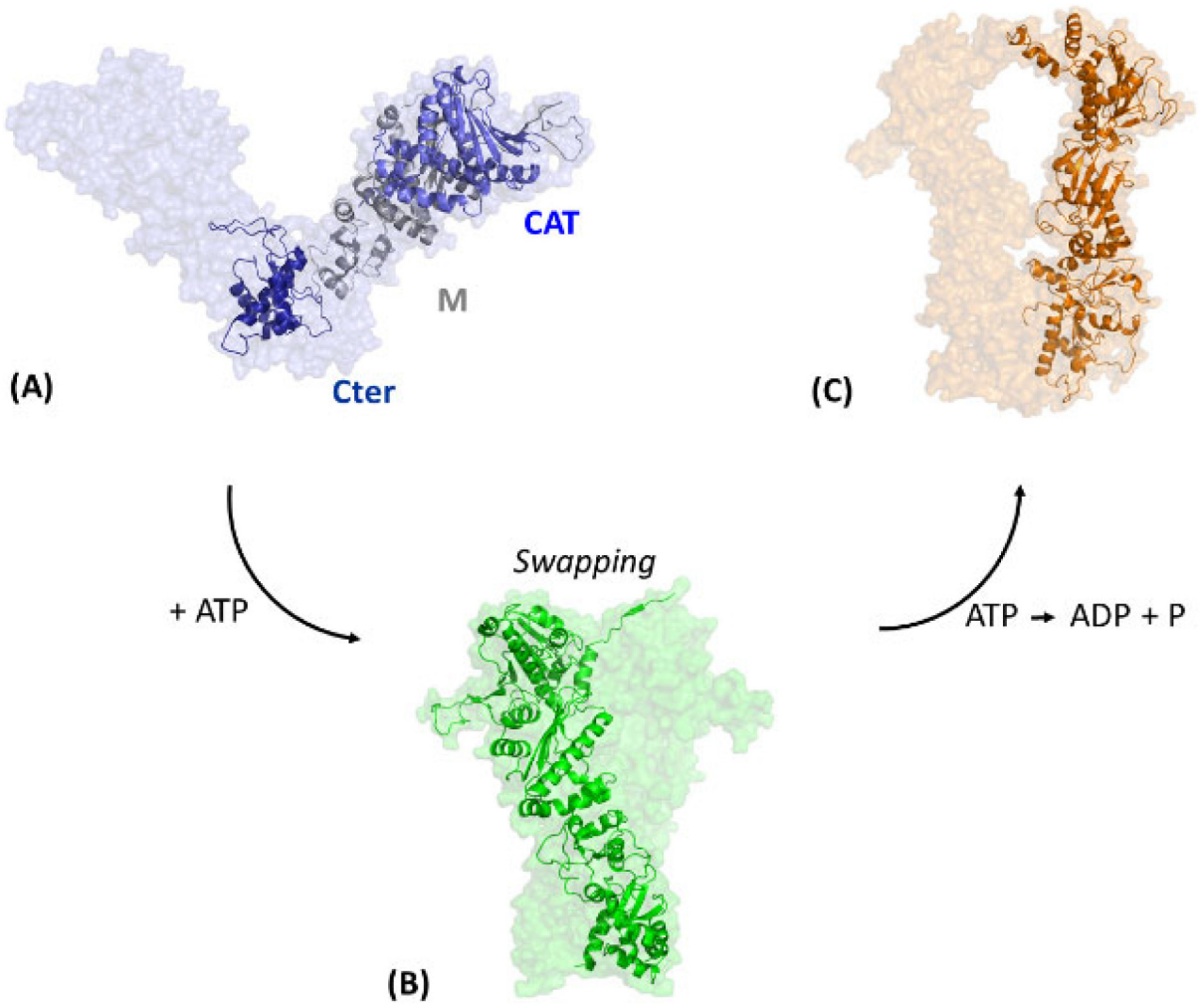

Fig. 4. Homology models of $HtpG_{Mtb}$ in its three binding states. Cartoon and surface representations of (A) $HtpG_{Mtb}$ free state, catalytic (CAT, residues 8–218), Middle (M, residues 219–505) and C-terminal (Cter, residues 506–644) domains are indicated in dark blue, grey and electric blue, respectively; (B) $HtpG_{Mtb}$ ATP-bound state, swapping of N-terminal strands is indicated; (C) $HtpG_{Mtb}$ ADP-bound state. In all representations, only one monomer is shown in cartoon, for clarity.

To better evaluate correlations between structural features and functional states and to gain further insights in the role of specific regions of the protein in this highly dynamic behavior of $HtpG_{Mtb}$, we used Molecular Dynamics simulations combined with cluster analysis.

3.3. Molecular dynamics studies corroborate the key role of the lid region in the clamping mechanism of HtpGMtb

We performed MD studies using as starting structures the regions 1–419 embedding the catalytic and the middle domains, in their free form (Cat-M-free) and in complex with ATP (Cat-M-ATP) to analyze the conformational behavior of $HtpG_{Mtb}$, depending on ATP binding.

The evaluation of root-mean-square deviations (RMSD) (calculated on the protein Cα atoms) between the starting models and the trajectory structures, shows large conformational variations, with RMSD values as large as about 0.8 nm for Cat-M-free and 0.7 nm for Cat-M-ATP (Fig. 5). To dissect conformational changes due to inter-domain movements from intra-domain rearrangements, we computed RMSD on isolated domains (Fig. 5A, B). In both binding states, it appears clear that main conformational changes are due to inter-domain motions and to a region, denoted as lid, which was previously found to change its conformation to allow nucleotide binding [43]. Indeed, in both free and ATP-bound $HtpG_{Mtb}$, RMSD values computed for individual domains after removing the N-terminal strand and lid region become close to 0.3 nm (Fig. 5A, B). A similar consideration can be applied to the ADP-bound state (Fig. 5C), although this aspect will be further described below.

Analysis of RMSF values, computed in an equilibrated region of trajectory (last 400 ns of the MD simulation), shows a strong correlation between the binding status of $HtpG_{Mtb}$ and its dynamic behavior. Namely, main differences in the catalytic site involve the lid region and the N-terminal strand, which display significantly higher RMSF values in the MD trajectory of the free enzyme, compared to the ATP bound and ADP bound states (Fig. 5D). Even higher RMSF values characterize the region 220–240, connecting the catalytic domain with the middle domain (Fig. 5D).

For a better understanding of correlations between protein conformations and binding states of the enzyme, average structures were computed for all simulations (Fig. 6). In the average ATP-bound structure, phosphate groups are tightly bound to the lid region, with hydrogen bonds which are stable throughout the MD simulation (Fig. S1). In particular, the γ-phosphate of ATP is cradled in a loop at the C-terminal side of the lid and forms hydrogen bonding with the peptide backbone of Gln125 and Gly127 and with the side chain of Arg353. These interactions contribute to conformationally constraining the lid region of the ATP bound state, as shown by its low RMSF values (Fig. 5D). The first helix of the lid in ATP bound state (102–109) is structurally conserved whereas it has a more transient nature in the free state (Fig. S2). In addition, the second helix in the ATP bound state is unwound, thus allowing the segment 125–129 to be well positioned to

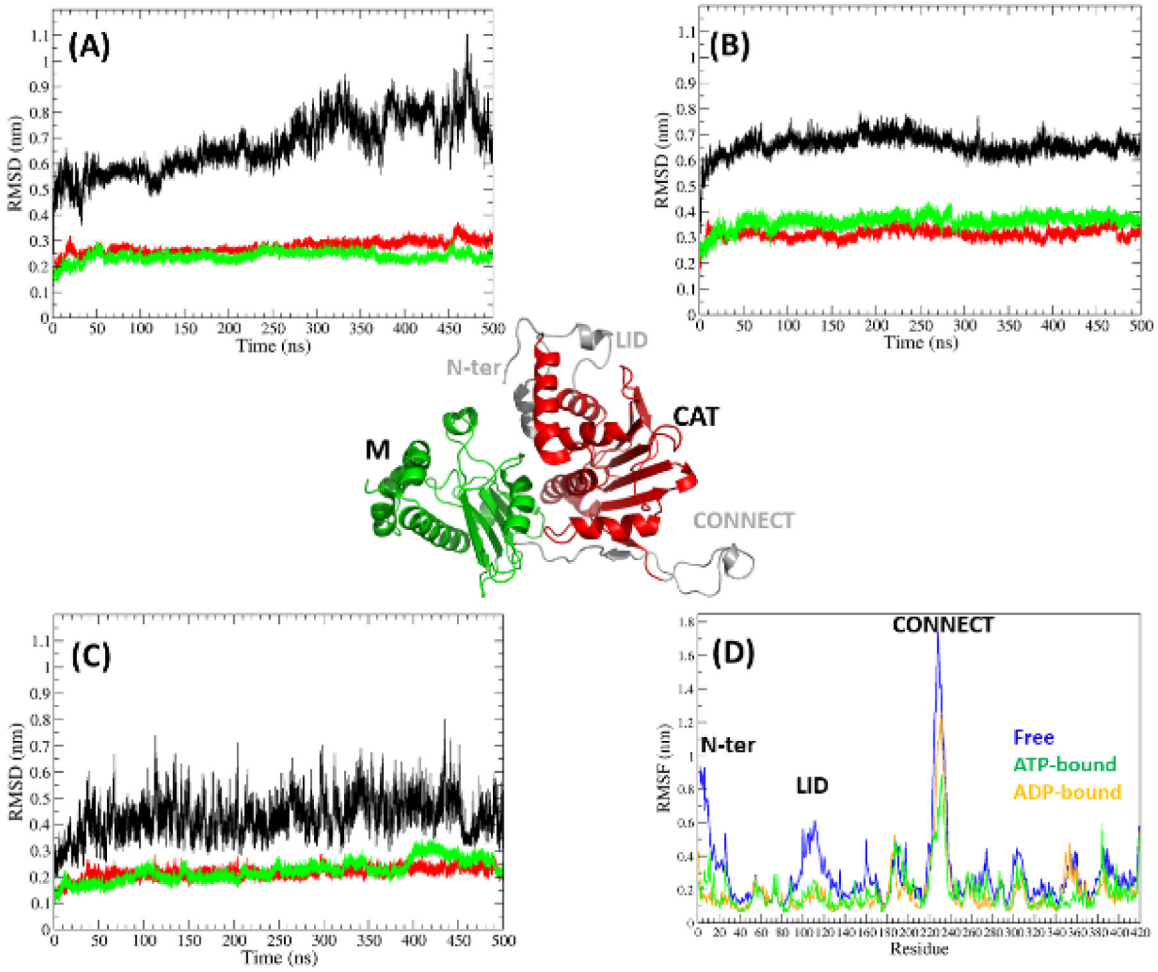

Fig. 5. RMSD and RMSF analysis from MD simulations. Time evolutions of RMSD (nm), computed on Cα atoms, for the simulation of (A) free, (B) ATP-bound and (C) ADP-bound states of the enzyme. Black lines correspond to all Cα, red lines to the catalytic domain deprived of the lid region (27–98, 130–219, CAT in the average structure reported in cartoon), green lines to the middle domain (250–419, M in the central cartoon). (D) RMSF values, calculated on backbone Cα atoms in the equilibrated region (50–500 ns) of for all trajectories. The color code is indicated. Regions with the highest RMSF, including the N-terminus (N-ter), the lid region (residues 99–129) and the connecting region between domains (CONNECT) are labeled.

interact with the ATP molecule (Fig. S1). In order to get a profitable binding with ATP, the segment 128–135 adopts a stable 3_{10} helix in ATP bound state, whereas in the free state is α-helical. The superposition of average structures of free and ATP bound forms clearly shows that a conformational switch occurs to the lid region upon ATP binding, as previously observed for other Hsps [43] (Fig. 6A). In MD dynamics of $HtpG_{Mtb}$, we observe the formation of tight interactions mediated in particular by the γ-phosphate groups of ATP, that lock the lid region in a conformation fully incompatible with the domain organization observed in the free form of the enzyme (Fig. 6B). Indeed, a large number of clashing interactions would form between the C-terminal part of the lid region and the middle domain (Table S1). Therefore, the observed strong rigidity of the lid region induced by ATP binding (Figs. 6, 7, S1, S2) and the incompatibility of the ATP-bound conformation of the lid with the domain organization observed in the free state provide a structural rationale to the overall rearrangement of the enzyme in the presence of ATP. As shown in Figs. 6C and 7, a complete reorientation of the catalytic and middle domains exists between the two average structures of the free and ATP-bound forms, involving a rotation of the middle domain of 119.5°, as computed by DynDom [44]. With this reorganization, the enzyme reaches a new conformation that completes the catalytic site, by bringing Arg353 in contact with the ATP γ-phosphate (Fig. 7). Indeed, the equivalent of Arg353 was previously proposed to be an essential catalytic residue in eukaryotic Hsp90 [45,46].

3.4. The structure of the free form of HtpGMtb is compatible with ADP binding

As shown in Fig. 6 and Table S1, the conformational state of the lid region in the ATP bound form of the enzyme is fully incompatible with the domain organization of the free enzyme. It is hitherto not clear whether binding of ADP is compatible with the conformation of the enzyme observed in the free state, since conflicting evidences are reported in the literature [43]. To attempt an answer to this question, we conducted MD studies integrated with clustering analysis. In detail, we performed extensive (1 μs) MD simulations of the catalytic domain of $HtpG_{Mtb}$ (residues 1–219) in complex with ADP (See Methods). These data confirmed a stable conformation of the lid in the presence of ADP, as observed for ATP, and the full conservation of its secondary structure elements (data not shown). With the goal to select only most representative conformers, we adopted a clustering procedure using the ptraj module of Amber [47]. The equilibrated part of the trajectory (300–1000 ns) sampled every 5 ps was used for the clustering. As a first result, the major cluster represented the 83% of sampled structures, followed by a poorly populated cluster, 8%. Therefore, we built a starting model for MD simulations by replacing residues 1–180 of the $HtpG_{Mtb}$ in its free state with those of the major cluster, to generate a model of $HtpG_{Mtb}$-ADP exhibiting the inter-domain organization observed in the structure of the free enzyme. 1 μs MD simulation of this model showed that this conformation is fully stable, and no major

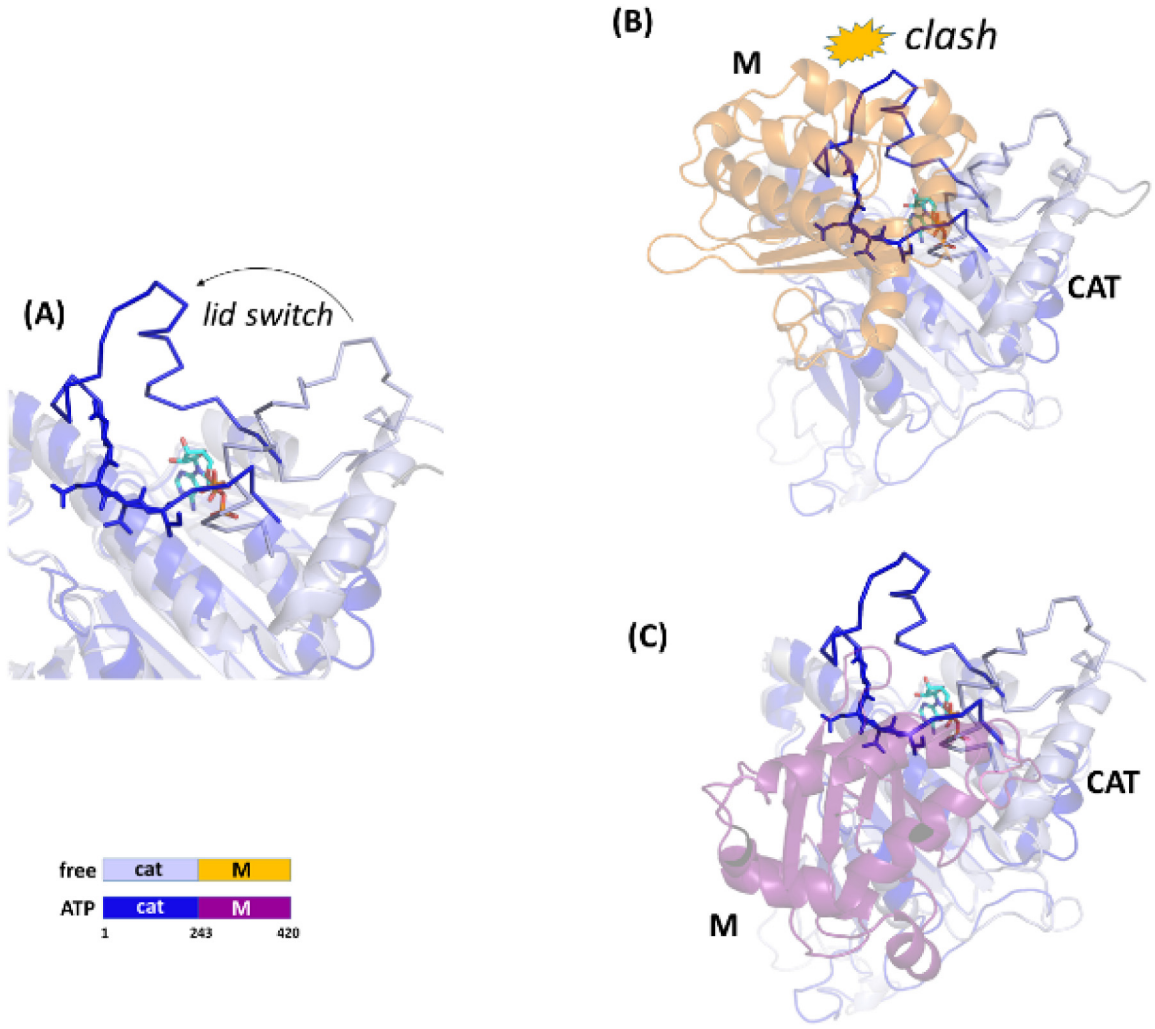

Fig. 6. The lid switch due to ATP binding is incompatible with the organization of domains in the free structure. Cartoon representation of average structures of free (light-blue/orange) and ATP bound (dark-blue/prune) states upon superposition of catalytic domains (light and dark-blue in free and ATP-bound, respectively). From the free to the ATP-bound form (A) the lid switches its conformation to form stable interactions with the ATP molecule (from light to dark-blue ribbon); (B) the switched conformation is incompatible with the conformation of M domain the free state (orange); (C) the M domain reorganizes by rotating 119° in the ATP-bound state (prune).

reorganizations of the enzyme conformation are observed along the trajectory as an effect of ADP binding. Different than observed of the free enzyme, this MD shows that the lid region remains conformationally stable, as indicated by the low RMSF values computed on these regions (Fig. 5D) and by the conservation of the lid helices 102–109 and 119–125 throughout the MD simulation (Fig. S2C). Superposition of average structures of the ADP bound and free forms shows a clear conformational switch of the lid region upon ADP binding, with the rotation of the lid of about 90 °C to close up the binding pocket (Fig. 8). Also, this ADP-driven switch involves the stabilization of helices 102–109 and 119–125, which have a transient nature in the free conformation (Fig. S2A). The ADP-bound conformation of the lid is located between the two domains and does not form conflicting interactions with the middle domain (Fig. 8). On the opposite, the lid strengthens the interaction between domains, by forming new H-bonds with the regions 272–274 and 300–303. These results unambiguously show that, different from what we observed for the ATP bound state, the local conformational change of the lid region of $HtpG_{Mtb}$ induced by the binding of ADP is fully compatible with the overall conformation of the free enzyme.

3.5. Structural determinants of HtpG-ESAT6Mtb low cytotoxicity

We previously proved that the fusion of $HtpG_{Mtb}$ to ESAT6 enhances the immunoreactivity of ESAT6 [27]. Also, beside exerting a durable BCG-prime boosting effect against hypervirulent HN878 in mice, this fused construct HtpG-$ESAT6_{Mtb}$ had another peculiar feature: it did not exert toxicity at 20 μg/mL, whereas ESAT6 showed cellular toxicity at a concentration above 5 μg/mL [27].

Mtb secretes ESAT6 as a heterodimeric complex ESAT6/CFP10 stabilized by hydrophobic interactions [48]. It was previously shown that in the absence of CFP10, the hydrophobic regions of the ESAT6 can form dimers/multimers, mimicking the ESAT6/CFP10 heterodimer [49,50]. In addition, their dissociation into monomers, obtained using the detergent ASB, generates a protein presenting entirely different activities [49]. Indeed, monomeric ESAT6 but not the multimeric one induced cell death and membrane pore formation whereas the dimeric ESAT6 behaved similarly to the physiological form of the complex ESAT6/CFP10 [49].

To investigate the correlation between the oligomerization state of HtpG-$ESAT6_{Mtb}$ and its cytotoxic properties, we evaluated the ability of ASB-treated and nontreated HtpG-$ESAT6_{Mtb}$ to inducing apoptosis. Prior to this study, we measured the concentration of ASB able to induce monomerization of HtpG-$ESAT6_{Mtb}$. As shown in Fig. 9A, we observed measurable amounts of monomeric protein using a protein to ASB ratio of 1:200, with an increase of monomer to dimer ratio at higher ASB concentrations. Using a 1:200 *ratio* of HtpG-$ESAT6_{Mtb}$ to ASB, we performed flow cytometric analysis with Annexin V and Propidium Iodide (PI) stain in comparison to non-treated HtpG-$ESAT6_{Mtb}$. As a result,

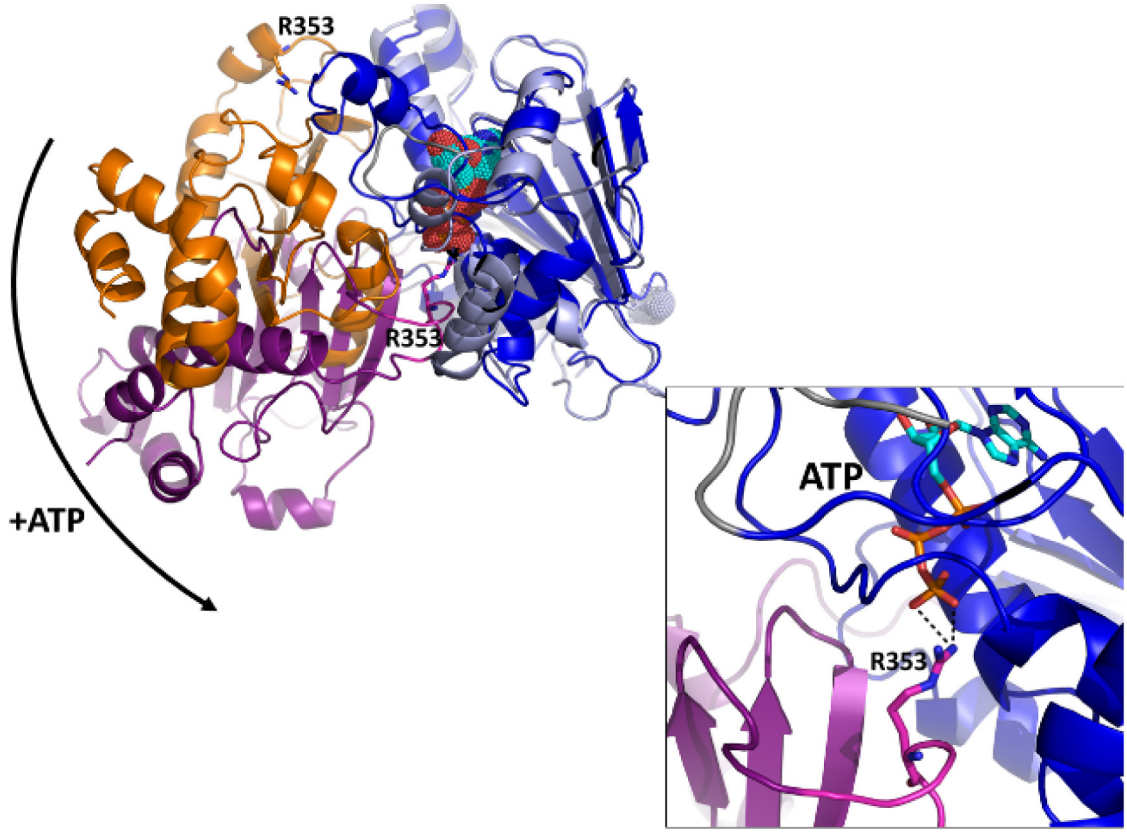

Fig. 7. ATP binding completes the catalytic site. Cartoon representation of average structures of free (light-blue/orange) and ATP bound (dark-blue/prune) states upon superposition of catalytic domains (light and dark-blue in free and ATP-bound, respectively). From the free to the ATP-bound form, the rotation of the middle domain (orange to prune) brings the catalytic Arg353 in the ATP binding site, as shown in the inset.

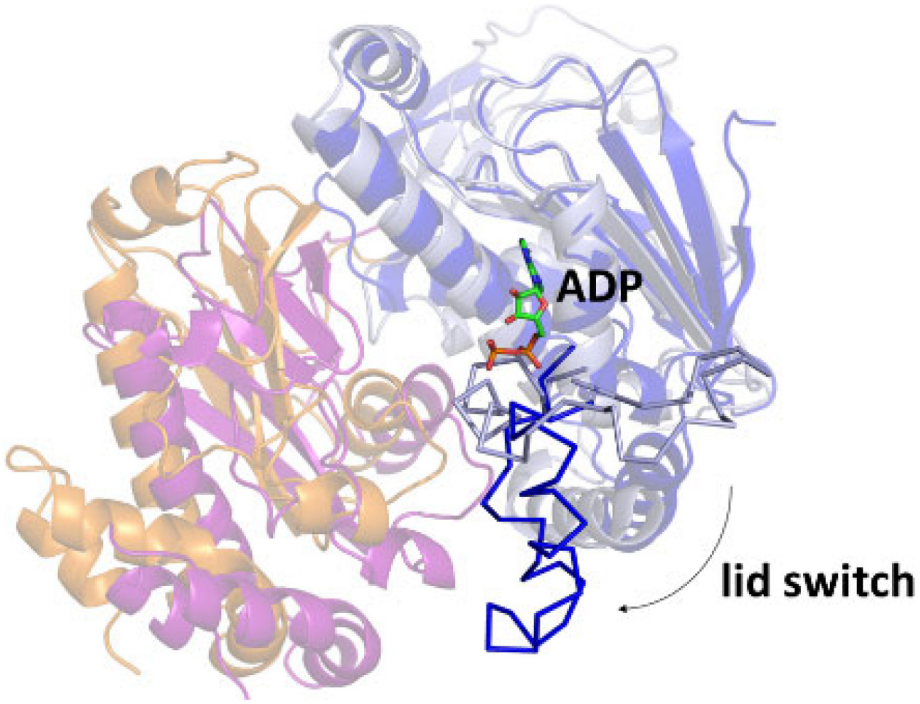

Fig. 8. ADP binding does not impose a structural reorganization of $HtpG_{Mtb}$. Cartoon representation of average structures of free (light-blue/orange) and ADP bound (dark-blue/prune) states after superposition of catalytic domains (light and dark-blue in free and ADP-bound, respectively). The lid region, in ribbon representation, switches upon ADP binding to reach a conformation compatible with the inter-domain organization of the free enzyme.

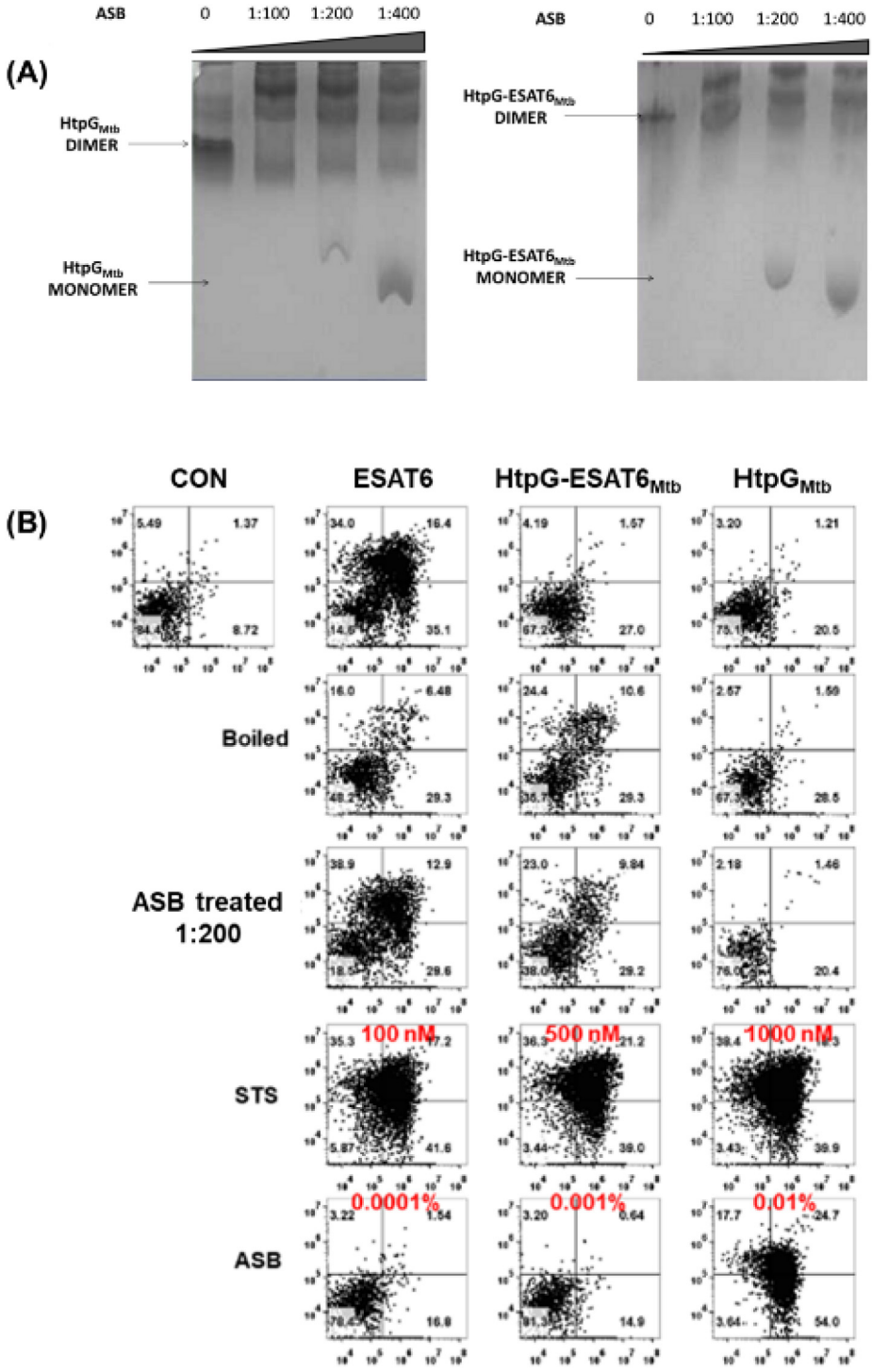

Fig. 9. Cytotoxicity of HtpG-ESAT6$_{Mtb}$ correlates with its oligomerization state. (A) Native gel electrophoresis of both HtpG$_{Mtb}$ and HtpG-ESAT6$_{Mtb}$ shows the formation of protein monomers using a protein:ASB ratio of 1:200. (B) ASB-treated HtpG-ESAT6$_{Mtb}$ but not the nontreated one induces cell death. Macrophages were treated with 5 μg/mL ESAT6, HtpG-ESAT6$_{Mtb}$ and HtpG$_{Mtb}$ for 24 h in the absence and in the presence of 0.0005% ASB (protein:ASB ratio 1:200). Cells were stained with annexin-V PI and analyzed by FACS. STS and ASB were used as controls.

we observed that only ASB-treated HtpG-ESAT6$_{Mtb}$ can induce macrophages death; treatment of cells with 5 μg/mL of ASB-treated HtpG-ESAT6$_{Mtb}$ resulted in 31.84% PI$^+$ cell population, of cell death. By contrast, non-treated HtpG-ESAT6$_{Mtb}$ did not affect cell survival (Fig. 9B). We also observed that the addition of ASB did not significantly alter cytotoxicity of the ESAT6 preparation, which caused apoptosis also in the absence of ASB. As a further control, we found that HtpG$_{Mtb}$ remains non cytotoxic also in the presence of ASB (Fig. 9B), a finding that proves that the gained cytotoxicity of HtpG-ESAT6$_{Mtb}$ upon ASB addition is due to the monomerization of the ESAT6 portion of the protein and not of the HtpG$_{Mtb}$ region.

To provide a structural rationalization to these findings, we homology modelled HtpG-ESAT6$_{Mtb}$. As shown in Fig. 10, HtpG$_{Mtb}$ and ESAT6 are properly organized in the fused HtpG-ESAT6$_{Mtb}$ protein to allow the antiparallel dimerization of ESAT6 helices, in a binding mode similar to that of the ESAT6/CFP10 heterodimer of Mtb (pdb code 3fav) and the homodimeric ESAT6 from *Geobacillus thermodenitrificans* (pdb code 3zbh) (Fig. S3). Therefore, the presence of HtpG$_{Mtb}$ at the N-terminal

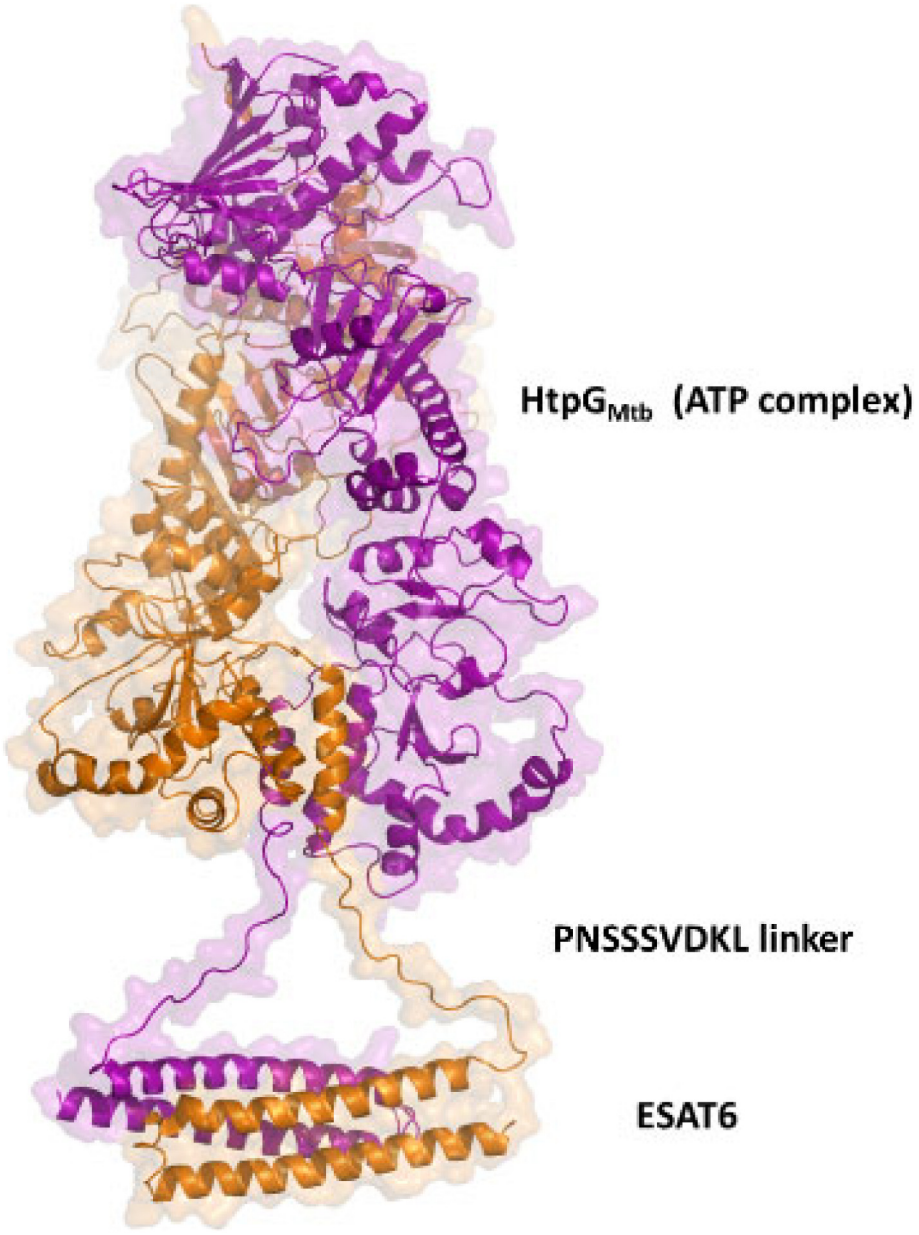

Fig. 10. Structural determinants of HtpG-ESAT6$_{Mtb}$ improved antigen properties. Cartoon and surface representation of the homology modeling structure of HtpG-ESAT6$_{Mtb}$ in its ATP bound state, obtained using MODELLER [28].

side of ESAT6 constrains ESAT6 in a dimeric state, which is known to be non-cytotoxic [49]. Namely, we suggest that in HtpG-ESAT6$_{Mtb}$, HtpG$_{Mtb}$ entropically favors the dimerization of ESAT6, in a way to mimic the conformation of the ESAT6/CFP10 heterodimer, therefore explaining the enhanced immunoreactivity and the hampered cytotoxicity of ESAT6 in the fused antigen [27].

4. Conclusion

All HtpG$_{Mtb}$ structural findings obtained here, including its secondary structure content and dimeric nature, the effect of AMP-PNP binding on the hydrodynamic radii, bioinformatic and MD analyses, point to the involvement of HtpG$_{Mtb}$ as a molecular chaperone in *M. tuberculosis*. Our data show that HtpG$_{Mtb}$ adopts a highly stable dimeric structure that strongly depends on its ligation state, as previously observed for other Hsps [39]. We observed that the dimeric nature of HtpG$_{Mtb}$, of fundamental importance for functional role of the clamping mechanism of Hsps, is not needed for structural stability. Indeed, CD and DLS data prove that HtpG$_{Mtb}$ monomerizes at 40 °C, with an associated decrease of its hydrodynamic radius from 6.7 Å to 4.4 Å, and remains highly stable as a monomer until the eventual unfolding occurs, at about 81 °C (Figs. 2, 3). The high stability of individual monomers is instrumental to the chaperone clamping mechanism, where the three domains must undergo rigid body movements from one to another functional state (Fig. 4). Homology modeling and dynamics provided a structural explanation to these experimental findings. They show that dramatic differences exist between each functional state and that both the free and the ATP bound states undergo inter-domain motions during the simulations, whereas individual domains remain highly stable (Fig. 5). During the ATP induced conformational change, a crucial role is played by the lid region, which adopts a rigid conformation throughout the MD simulations, mainly due to the multiple interactions of its C-terminal end with the γ-phosphate of ATP (Fig. S1). This finding is the key to understand the incompatibility of ATP binding with the structure of the enzyme in the free state, since severe unfavorable interactions mediated by the lid would make the free conformation of the enzyme completely

inaccessible (Fig. 6 and Table S1). MD studies also highlighted that the local conformational changes due to ADP binding can be fully absorbed by the catalytic domain and are compatible with the structure of the free enzyme (Fig. 8), suggesting that once ATP is hydrolyzed, $HtpG_{Mtb}$ reorganizes in an open conformation, as observed in the free state, and the enzyme is again able to accommodate new client proteins.

Structural features of $HtpG_{Mtb}$ are consistent with its ability to induce DC maturation and to exert antimycobacterial action through DC activation [27]. Indeed, Heat Shock Proteins are known to modulate the immune system by stimulating both innate and adaptive responses [51]. The term 'chaperokine' has been used to describe the dual activity of Heat Shock Proteins functioning as both chaperone and cytokine [51]. Most importantly, our data provide an explanation to the enhanced antigenic properties of the fused HtpG-$ESAT6_{Mtb}$ compared to $HtpG_{Mtb}$. Indeed, we show that a strong correlation exists between the oligomeric state of this antigen and its cytotoxicity properties. As previously observed for ESAT6, HtpG-$ESAT6_{Mtb}$ becomes cytotoxic upon monomerization (Fig. 9). Overall, our data suggest that not only does the fused HtpG-$ESAT6_{Mtb}$ combine the antigenic properties of $HtpG_{Mtb}$ and ESAT6, but $HtpG_{Mtb}$ plays also the role of hampering ESAT6 cytotoxicity by favoring its dimerization (Fig. 10).

Acknowledgments

This work was supported by the project 2017SFBFER funded by the Italian MIUR. Authors also acknowledge the Italian Cooperation Program with the National Research Foundation of Korea "Structure and immunogenic function of a promising vaccine against Tuberculosis", 2018–2019, and the Cooperation program managed by the National Research Foundation of Korea (2017K2A9A1A06037583). The authors thank Luca De Luca and Maurizio Amendola for technical support. CINECA Supercomputing (framework ISCRA@CINECA—project codes HP10CVGBTL) is acknowledged for computational support.

Author contributions

Miguel Moreira: Conceptualization, Methodology. **Alessia Ruggiero:** Supervision, Data curation, Methodology. **Luciana Esposito:** Data curation, Investigation. **Han-Gyu Choi:** Investigation. **Hwa-Jung Kim:** Investigation and writing. **Rita Berisio:** Writing- Reviewing and Editing,

Appendix A. Supplementary data

Supplementary data to this article can be found online at https://doi.org/10.1016/j.ijbiomac.2020.04.252.

References

[1] W. Cruz-Knight, L. Blake-Gumbs, Tuberculosis: an overview, Prim Care 40 (3) (2013) 743–756.
[2] N. Fogel, Tuberculosis: a disease without boundaries, Tuberculosis (Edinb) 95 (5) (2015) 527–531.
[3] G. Delogu, M. Sali, G. Fadda, The biology of mycobacterium tuberculosis infection, Mediterr. J. Hematol. Infect. Dis. 5 (1) (2013), e2013070. .
[4] F. De Maio, F. Squeglia, D. Goletti, G. Delogu, The mycobacterial HBHA protein: a promising biomarker for tuberculosis, Curr. Med. Chem. 26 (11) (2019) 2051–2060.
[5] C. Esposito, M.V. Pethoukov, D.I. Svergun, A. Ruggiero, C. Pedone, E. Pedone, R. Berisio, Evidence for an elongated dimeric structure of heparin-binding hemagglutinin from mycobacterium tuberculosis, J. Bacteriol. 190 (13) (2008) 4749–4753.
[6] F. Squeglia, A. Ruggiero, A. De Simone, R. Berisio, A structural overview of mycobacterial adhesins: key biomarkers for diagnostics and therapeutics, Protein Sci. 27 (2) (2018) 369–380.
[7] M. Pai, M.A. Behr, D. Dowdy, K. Dheda, M. Divangahi, C.C. Boehme, A. Ginsberg, S. Swaminathan, M. Spigelman, H. Getahun, D. Menzies, M. Raviglione, Tuberculosis, Nat. Rev. Dis. Primers. 2 (2016), 16076. .
[8] F. Squeglia, A. Ruggiero, R. Berisio, Chemistry of peptidoglycan in mycobacterium tuberculosis life cycle: an off-the-wall balance of synthesis and degradation, Chemistry 24 (11) (2018) 2533–2546.
[9] A. Ruggiero, F. Squeglia, M. Romano, L. Vitagliano, A. De Simone, R. Berisio, Structure and dynamics of the multi-domain resuscitation promoting factor RpfB from mycobacterium tuberculosis, J. Biomol. Struct. Dyn. 35 (6) (2017) 1322–1330.
[10] V. Maione, A. Ruggiero, L. Russo, A. De Simone, P.V. Pedone, G. Malgieri, R. Berisio, C. Isernia, NMR structure and dynamics of the resuscitation promoting factor RpfC catalytic domain, PLoS One 10 (11) (2015), e0142807. .
[11] A. Ruggiero, F. Squeglia, M. Romano, L. Vitagliano, A. De Simone, R. Berisio, The structure of resuscitation promoting factor B from M. tuberculosis reveals unexpected ubiquitin-like domains, Biochim. Biophys. Acta 1860 (2) (2016) 445–451.
[12] V.D. Nikitushkin, G.R. Demina, M.O. Shleeva, S.V. Guryanova, A. Ruggiero, R. Berisio, A.S. Kaprelyants, A product of RpfB and RipA joint enzymatic action promotes the resuscitation of dormant mycobacteria, FEBS J. 282 (13) (2015) 2500–2511.
[13] F. Squeglia, A. Ruggiero, R. Berisio, Exit from mycobacterial dormancy: a structural perspective, Curr. Med. Chem. 22 (14) (2015) 1698–1709.
[14] F. Squeglia, R. Marchetti, A. Ruggiero, R. Lanzetta, D. Marasco, J. Dworkin, M. Petoukhov, A. Molinaro, R. Berisio, A. Silipo, Chemical basis of peptidoglycan discrimination by PrkC, a key kinase involved in bacterial resuscitation from dormancy, J. Am. Chem. Soc. 133 (51) (2011) 20676–20679.
[15] E.G. Salina, A.S. Grigorov, O.S. Bychenko, Y.V. Skvortsova, I.Z. Mamedov, T.L. Azhikina, A.S. Kaprelyants, Resuscitation of dormant "non-culturable" mycobacterium tuberculosis is characterized by immediate transcriptional burst, Front. Cell. Infect. Microbiol. 9 (2019) 272.
[16] V.D. Nikitushkin, G.R. Demina, A.S. Kaprelyants, Rpf proteins are the factors of reactivation of the dormant forms of Actinobacteria, Biochemistry (Mosc) 81 (13) (2016) 1719–1734.
[17] P. Andersen, S.H. Kaufmann, Novel vaccination strategies against tuberculosis, Cold Spring Harb. Perspect. Med. 4 (6) (2014).
[18] B.M. Buddle, N.A. Parlane, D.N. Wedlock, A. Heiser, Overview of vaccination trials for control of tuberculosis in cattle, wildlife and humans, Transbound. Emerg. Dis. 60 (Suppl. 1) (2013) 136–146.
[19] M. Favorov, M. Ali, A. Tursunbayeva, I. Aitmagambetova, P. Kilgore, S. Ismailov, T. Chorba, Comparative tuberculosis (TB) prevention effectiveness in children of Bacillus Calmette-Guerin (BCG) vaccines from different sources, Kazakhstan, PLoS One 7 (3) (2012), e32567. .
[20] C. Franco-Paredes, N. Rouphael, C. del Rio, J.I. Santos-Preciado, Vaccination strategies to prevent tuberculosis in the new millennium: from BCG to new vaccine candidates, Int. J. Infect. Dis. 10 (2) (2006) 93–102.
[21] G. Singh, P. Kesharwani, A.K. Srivastava, Tuberculosis treated by multiple drugs: an overview, Curr. Drug Deliv. 15 (3) (2018) 312–320.
[22] N. Gupta, S. Garg, S. Vedi, D.Y. Kunimoto, R. Kumar, B. Agrawal, Future path toward TB vaccine development: boosting BCG or re-educating by a new subunit vaccine, Front. Immunol. 9 (2018) 2371.
[23] P. Brodin, K. Eiglmeier, M. Marmiesse, A. Billault, T. Garnier, S. Niemann, S.T. Cole, R. Brosch, Bacterial artificial chromosome-based comparative genomic analysis identifies Mycobacterium microti as a natural ESAT-6 deletion mutant, Infect. Immun. 70 (10) (2002) 5568–5578.
[24] B. Samten, X. Wang, P.F. Barnes, Immune regulatory activities of early secreted antigenic target of 6-kD protein of Mycobacterium tuberculosis and implications for tuberculosis vaccine design, Tuberculosis (Edinb) 91 (Suppl. 1) (2011) S114–S118.
[25] C. Aagaard, T. Hoang, J. Dietrich, P.J. Cardona, A. Izzo, G. Dolganov, G.K. Schoolnik, J.P. Cassidy, R. Billeskov, P. Andersen, A multistage tuberculosis vaccine that confers efficient protection before and after exposure, Nat. Med. 17 (2) (2011) 189–194.
[26] D.T. Loots, C.C. Swanepoel, M. Newton-Foot, N.C. Gey van Pittius, A metabolomics investigation of the function of the ESX-1 gene cluster in mycobacteria, Microb. Pathog. 100 (2016) 268–275.
[27] H.G. Choi, S. Choi, Y.W. Back, S. Paik, H.S. Park, W.S. Kim, H. Kim, S.B. Cha, C.H. Choi, S.J. Shin, H.J. Kim, Rv2299c, a novel dendritic cell-activating antigen of Mycobacterium tuberculosis, fused-ESAT-6 subunit vaccine confers improved and durable protection against the hypervirulent strain HN878 in mice, Oncotarget 8 (12) (2017) 19947–19967.
[28] B. Webb, A. Sali, Protein structure modeling with MODELLER, Methods Mol. Biol. 1654 (2017) 39–54.
[29] D. Van Der Spoel, E. Lindahl, B. Hess, G. Groenhof, A.E. Mark, H.J. Berendsen, GROMACS: fast, flexible, and free, J. Comput. Chem. 26 (16) (2005) 1701–1718.
[30] F. Squeglia, M. Romano, A. Ruggiero, L. Vitagliano, A. De Simone, R. Berisio, Carbohydrate recognition by RpfB from mycobacterium tuberculosis unveiled by crystallographic and molecular dynamics analyses, Biophys. J. 104 (11) (2013) 2530–2539.
[31] A. Ruggiero, J. Marchant, F. Squeglia, V. Makarov, A. De Simone, R. Berisio, Molecular determinants of inactivation of the resuscitation promoting factor B from mycobacterium tuberculosis, J. Biomol. Struct. Dyn. 31 (2) (2013) 195–205.
[32] W.L. Jorgensen, D.S. Maxwell, J. TiradoRives, Development and testing of the OPLS all-atom force field on conformational energetics and properties of organic liquids, J. Am. Chem. Soc. 118 (45) (1996) 11225–11236.
[33] G.A. Kaminski, R.A. Friesner, J. Tirado-Rives, W.L. Jorgensen, Evaluation and reparametrization of the OPLS-AA force field for proteins via comparison with accurate quantum chemical calculations on peptides, J. Phys. Chem. B 105 (28) (2001) 6474–6487.
[34] B. Hess, H. Bekker, H.J.C. Berendsen, J.G.E.M. Fraaije, LINCS: a linear constraint solver for molecular simulations, J. Comput. Chem. 18 (12) (1997) 1463–1472.
[35] T. Darden, D. York, L. Pedersen, Particle mesh Ewald - an n.log(N) method for Ewald sums in large systems, J. Chem. Phys. 98 (12) (1993) 10089–10092.
[36] W. Humphrey, A. Dalke, K. Schulten, VMD: Visual molecular dynamics, J. Mol. Graph Model. 14 (1) (1996) 33–38.
[37] K.L. Meagher, L.T. Redman, H.A. Carlson, Development of polyphosphate parameters for use with the AMBER force field, J. Comput. Chem. 24 (9) (2003) 1016–1025.

[38] M.M. Ali, S.M. Roe, C.K. Vaughan, P. Meyer, B. Panaretou, P.W. Piper, C. Prodromou, L.H. Pearl, Crystal structure of an Hsp90-nucleotide-p23/Sba1 closed chaperone complex, Nature 440 (7087) (2006) 1013–1017.
[39] F.H. Schopf, M.M. Biebl, J. Buchner, The HSP90 chaperone machinery, Nat. Rev. Mol. Cell Biol. 18 (6) (2017) 345–360.
[40] A. Balasubramanian, M. Markovski, J.R. Hoskins, S.M. Doyle, S. Wickner, Hsp90 of E. coli modulates assembly of FtsZ, the bacterial tubulin homolog, Proc. Natl. Acad. Sci. U. S. A. 116 (25) (2019) 12285–12294.
[41] F. Squeglia, M. Moreira, A. Ruggiero, R. Berisio, The Cell Wall hydrolytic NlpC/P60 Endopeptidases in mycobacterial cytokinesis: a structural perspective, Cells 8 (6) (2019).
[42] A.K. Shiau, S.F. Harris, D.R. Southworth, D.A. Agard, Structural analysis of E. coli hsp90 reveals dramatic nucleotide-dependent conformational rearrangements, Cell 127 (2) (2006) 329–340.
[43] L.H. Pearl, Review: the HSP90 molecular chaperone-an enigmatic ATPase, Biopolymers 105 (8) (2016) 594–607.
[44] R.A. Lee, M. Razaz, S. Hayward, The DynDom database of protein domain motions, Bioinformatics 19 (10) (2003) 1290–1291.
[45] P. Meyer, C. Prodromou, C. Liao, B. Hu, S. Mark Roe, C.K. Vaughan, I. Vlasic, B. Panaretou, P.W. Piper, L.H. Pearl, Structural basis for recruitment of the ATPase activator Aha1 to the Hsp90 chaperone machinery, EMBO J. 23 (3) (2004) 511–519.
[46] P. Meyer, C. Prodromou, B. Hu, C. Vaughan, S.M. Roe, B. Panaretou, P.W. Piper, L.H. Pearl, Structural and functional analysis of the middle segment of hsp90: implications for ATP hydrolysis and client protein and cochaperone interactions, Mol. Cell 11 (3) (2003) 647–658.
[47] D.R. Roe, T.E. Cheatham 3rd, PTRAJ and CPPTRAJ: software for processing and analysis of molecular dynamics trajectory data, J. Chem. Theory Comput. 9 (7) (2013) 3084–3095.
[48] C. Poulsen, S. Panjikar, S.J. Holton, M. Wilmanns, Y.H. Song, WXG100 protein superfamily consists of three subfamilies and exhibits an alpha-helical C-terminal conserved residue pattern, PLoS One 9 (2) (2014), e89313. .
[49] A. Refai, M. Haoues, H. Othman, M.R. Barbouche, P. Moua, A. Bondon, L. Mouret, N. Srairi-Abid, M. Essafi, Two distinct conformational states of Mycobacterium tuberculosis virulent factor early secreted antigenic target 6 kDa are behind the discrepancy around its biological functions, FEBS J. 282 (21) (2015) 4114–4129.
[50] J. Teutschbein, G. Schumann, U. Mollmann, S. Grabley, S.T. Cole, T. Munder, A protein linkage map of the ESAT-6 secretion system 1 (ESX-1) of Mycobacterium tuberculosis, Microbiol. Res. 164 (3) (2009) 253–259.
[51] S. McNulty, C.A. Colaco, L.E. Blandford, C.R. Bailey, S. Baschieri, S. Todryk, Heat-shock proteins as dendritic cell-targeting vaccines—getting warmer, Immunology 139 (4) (2013) 407–415.